Constraints on asteroid magnetic field evolution and the radii of meteorite parent bodies from thermal modelling

James F J Bryson

Department of Earth Sciences, University of Cambridge, Cambridge, UK

Jerome A Neufeld

BP Institute, University of Cambridge, Cambridge, UK

Bullard Laboratories, Department of Earth Sciences, University of Cambridge, Cambridge, UK

Department of Applied Mathematics and Theoretical Physics, University of Cambridge, Cambridge, UK

Francis Nimmo

Department of Earth and Planetary Sciences, University of California, Santa Cruz, California, USA

Abstract

Paleomagnetic measurements of ancient terrestrial and extraterrestrial samples indicate that numerous planetary bodies generated magnetic fields through core dynamo activity during the early solar system. The existence, timing, intensity and stability of these fields are governed by the internal transfer of heat throughout their parent bodies. Thus, paleomagnetic records preserved in natural samples can contain key information regarding the accretion and thermochemical history of the rocky bodies in our solar system. However, models capable of predicting these field properties across the entire active lifetime of a planetary core that could relate the processes occurring within these bodies to features in these records and provide such information are limited. Here, we perform asteroid thermal evolution models across suites of radii, accretion times and thermal diffusivities with the aim of predicting when fully and partially differentiated asteroids generated magnetic fields. We find that dynamo activity in both types of asteroid is delayed until ~4.5 - 5.5 Myr after calcium-aluminium-rich inclusion formation due to the partitioning of ^{26}Al into the silicate portion of the body during differentiation and large early surface heat fluxes, followed by a brief period (<12.5 Myr for bodies with radii <500 km) of thermally-driven dynamo activity as heat is convected from the core across a partially-molten magma ocean. We also expect that gradual core solidification produced compositionally-driven dynamo activity in these bodies, the timing of which could vary by tens to hundreds of millions of years depending on the S concentration of the core and the radius of the body. There was likely a pause in core cooling and dynamo activity following the cessation of convection in the magma ocean. Our predicted periods of magnetic field generation and quiescence match eras of high and low paleointensities in the asteroid magnetic field record compiled from paleomagnetic measurements of multiple meteorites, providing the possible origins of the remanent magnetisations carried by these samples. We also compare our predictions to paleomagnetic results from different meteorite groups to constrain the radii of the angrite, CV chondrite, H chondrite, IIE iron meteorite and Bjürbole (L/LL chondrite) parent bodies and identify a nebula origin for the remanent magnetisation carried by the CM chondrites.

---

1. Introduction

Of the tens of thousands of rocky planetary bodies in our solar system, only Earth, Mercury, Ganymede and possibly Io are generating detectable magnetic fields through core dynamo activity at the present day (Stevenson, 2010). However, paleomagnetic measurements of samples from the Moon (Garrick-Bethell et al., 2009; Tikoo et al., 2017), Mars (Weiss et al., 2008) and numerous asteroids (Carporzen et al., 2011; Fu et al., 2012; Bryson et al., 2015, 2017; Wang et al., 2017) indicate that all of these bodies generated magnetic fields during the first few tens to hundred million years of the solar system (Weiss et al., 2010). Measurements of ancient terrestrial samples also suggest that Earth has generated a continuous magnetic field for at least the last $\sim$3.5 Gyr (Tarduno et al., 2010) and measurements made by the MESSENGER mission demonstrate that Mercury generated a field $>$3.7 Gyr ago (Johnson et al., 2015). Together, these observations indicate that dynamo activity and planetary magnetic fields were widespread among both large and small rocky bodies during the early solar system.

Planetary magnetic fields are generated by the organised motion of molten metal within a planetary core. The earliest process thought to induce this motion within the cores of asteroid-sized bodies is the direct extraction of heat as the body cooled (Sterenborg and Crowley, 2013). This thermally-driven convection occurs when the heat flux out of the core is larger than the adiabatic heat flux across the core, which is expected to have only been the case during the first $\sim$10 - 50 Myr after the formation of calcium-aluminium-rich inclusions (CAIs, the oldest solids in the solar system) depending on the size of the body (Elkins-Tanton et al., 2011). Core cooling is a relatively inefficient mechanism of dynamo generation (Nimmo, 2009), likely only producing magnetic fields for a portion of this period (Sterenborg and Crowley, 2013). Core convection can also result from chemical segregation within the core liquid, which can be induced by gradual core solidification. This compositionally-driven convection only occurs once an asteroid core cools to its freezing temperature, which will depend predominantly on its S concentration and can range between ~1800 - 1200 K (Scheinberg et al., 2016). The low pressures within an asteroid could result in either inward or outward core solidification, also depending critically on the S concentration of the core liquid (Williams, 2009). During outward core solidification at sub-eutectic S concentrations, S is rejected from the advancing solid and becomes enriched in the core liquid at the inner core boundary, introducing a gravitationally-unstable density stratification that causes convection. During inward core solidification, convection could be driven by the solidification, sinking and melting of micron-scale Fe crystals (more likely in slower-cooled, mantled cores; Ruckriemen et al., 2015) or the delamination of iron diapirs from a metallic crust at the surface of the core (more likely in faster-cooled, unmantled cores; Neufeld et al., 2019). Core solidification is an efficient mechanism of dynamo generation (Nimmo, 2009) with models suggesting this process possibly generates magnetic fields for prolonged periods during core solidification, which was probably a few tens of Myr depending on the size of the core (Bryson et al., 2015). Both core solidification regimes have been proposed as the origin of magnetic activity within asteroid sized bodies (Bryson et al., 2015, 2017).

The properties of a core dynamo are therefore governed by the internal transfer of heat throughout a planetary body, so the timing of magnetic field generation gleaned from paleomagnetic measurements can be used to constrain the thermal, chemical and structural history of a planetary body. The asteroid magnetic field record compiled from measurements of the remanent magnetisation carried by a variety of meteorites (including chondrites, rocky achondrites, stony-iron meteorites and iron meteorites) has steadily grown over the past few decades and potentially contains a wealth of information regarding the physical properties and thermochemical evolution of asteroids. However, models capable of relating the processes occurring throughout the evolution of an asteroid to the features in this record that could provide such information are limited. Here, we model the thermal evolution of asteroids across the entire active lifetimes of their core with the aim of predicting their timing of dynamo generation. We build on previous modelling studies of asteroid dynamo generation (Elkins-Tanton et al., 2011; Sterenborg and Crowley, 2013; Bryson et al., 2015) by performing simulations that consider multiple mechanisms of dynamo generation and cover suites of asteroid radii, accretion times and thermal diffusivities, allowing us to identify the effects of the physical properties of a body on its dynamo activity. We also model the thermal evolution of bodies that reached their final radius in two discrete accretion events to investigate the structure and timing of dynamo activity in the resultant bodies. Finally, we compare our model predictions to the timing of magnetic field generation recovered from paleomagnetic measurements of a range of meteorite groups, including the angrites (Wang et al., 2017), H chondrites (Bryson et al., in press), IIE irons (Maurel et al., 2018), Bjürbole (L/LL chondrite, Shah et al., 2017), CV chondrites (Carporzen et al., 2011; Fu et al., 2014a; Gattacceca et al., 2016; Shah et al., 2017) and CM chondrites (Cournede et al., 2015) with the goal of predicting the processes that generated the fields that magnetised these meteorites and constraining the thermochemical evolution and physical properties of their parent asteroids.

2. Thermal Evolution Models

2.1. Modelling approach

We choose to adopt a relatively straightforward and idealised iterative model of asteroid thermal evolution. Despite simplifications, our model captures much of the key physics of radiogenic heat production and transport and allows us to draw constraints on the timing of dynamo activity and explore its behaviour over a wide range of parameters. An example of the straightforward nature of our model is our treatment of core solidification. The compositions of iron meteorites indicate that the S concentrations of asteroid cores spanned the sub-eutectic range (i.e., $0 < \mathrm{S\ wt\%} < 32$; Goldstein et al., 2009). The S concentration of a specific asteroid core will depend on the nature of metal and silicate equilibration during melting and differentiation, the inclusion of which is beyond the scope of this study. Hence, we assumed the S concentration of the cores in all our models was the eutectic value (32 wt%) such that the cores solidified during a single process at 1200 K (Bryson et al., 2015). In reality, the sub-eutectic S concentrations of most asteroid cores will have led to initial solidification at higher temperatures (~1800 - 1200 K) and earlier times than those predicted by our model (Scheinberg et al., 2016). Asteroid cores with sub-eutectic S concentrations could have undergone periods of cooling (when the core temperature was greater than its freezing temperature), contemporaneously solidifying and cooling (when the core was at its freezing temperature for off-eutectic compositions), and only solidifying (when the core temperature was at the eutectic temperature). Compositionally-driven convection can only be generated in outwardly-solidifying cores during the period of contemporaneous cooling and solidification. Inward core solidification is thought to have induced compositional convection through fundamentally different mechanisms to outward solidification, so dynamo activity might have been generated during different phases of inward core solidification. Given the uncertainties surrounding the directions and start time of asteroid core solidification, we are unable to predict the timing of compositionally-driven convection from our model, although we do expect this process could have generated magnetic fields for at least a portion of core solidification (see Supplementary Material). For eutectic and sub-eutectic concentrations (excluding pure Fe), core solidification ends once the specific heat required to cool the core to 1200 K and the latent heat of solidifying its entire volume have been extracted from the core. The values of these heats are independent of core S concentrations in this range, so we are able to predict the end time of core solidification from our models. It is also possible that the core initial melt fraction could influence the end time of its solidification (e.g., Neumann et al., 2014).

The mathematical description of our model is included in the Supplementary Material and the values of all of the model parameters are presented in Table 1. We considered two mechanisms of asteroid accretion: a body forms to its final radius instantaneously during a single accretion event, and a body forms to its final radius in two discrete, instantaneous accretion events. Each of these events involves the accretion of billions of chondrules, CAIs and dust. The first mechanism is believed to result in either entirely differentiated or completely undifferentiated bodies depending on the time of accretion relative to CAI formation (Weiss and Elkins-Tanton, 2013). The second mechanism has been suggested as a likely asteroid growth mechanism for bodies with radii >100 km (Johansen et al., 2015) and could have created partially differentiated bodies consisting of a molten interior that forms from the material accreted during the first accretion event that is encased by chondritic material added during the second accretion event (Elkins-Tanton et al., 2011; Bryson et al., in press). Collisions between planetesimals could also have resulted in their growth, however we do not model this process as it has not been proposed as a explanation of the magnetisation of chondrites (Elkins-Tanton et al., 2011). Some asteroid thermal evolution models can produce partially differentiated bodies through single accretion at ∼1 - 2 Myr after CAI formation (Lichtenberg et al., 2018), however we did not consider this mechanism in this study.

2.2. Model details

In our single accretion event model, we investigated the effect of planetary radius, r_1, accretion time, t_1, and thermal diffusivity, κ, on the evolution of asteroid dynamo activity (see Supplementary Material). We performed 10,000 models with randomly chosen combinations of r_1 between 20 - 500 km [ranging from the approximate minimum radius for differentiation (Hevey and Sanders, 2006) up to a radius greater than any body in the asteroid belt at the present day] and t_1 between 0.0 - 2.0 Myr after CAI formation (encompassing the period that sufficient radiogenic abundances were incorporated into asteroids so they could have differentiated) for a given κ value. The thermal diffusivity of unmetamorphosed, porous chondritic material is $\sim 3 \times 10^{-7}$ m^2 s^{-1}, which we took as the value of freshly accreted material in all our models (Opeil et al., 2012). The cold (∼200 K) surface of rocky planetesimals is likely composed of a porous, insulating regolith that is expected to have a thermal diffusivity similar to this material (Warren, 2011), while the material at depth is expected to sinter and display higher thermal diffusivities. We approximate regolith production and sintering (see Supplementary Material) by increasing the κ value of any material that exceeds 700 K (Yomogida and Matsui, 1984) to either 6×10^{-7} m^2 s^{-1}(nominally the diffusivity of CV chondrites), 9×10^{-7} m^2 s^{-1}(nominally the diffusivity of ordinary chondrites and rocky achondrites), or 12×10^{-7} m^2 s^{-1}(nominally the thermal diffusivity of enstatite chondrites) depending on the simulation (Opeil et al., 2012). Based on the approximate volume fraction of metal in the ordinary and enstatite chondrites (Scott, 2007), we modelled the radius of the core, r_c, as half the radius of the molten portion of the body. Our simulations lasted for 240,000 timesteps, which corresponds to ∼760 Myr. The temperature of the material immediately after it accreted is 200 K (Henke et al., 2013).

In our two accretion event model, a body forms with an initial radius, r_1, at an early time, t_1, during the first accretion event, and at a later time, t_2, the radius increases to its final value, r_2, by the addition of cold chondrules, CAIs and dust to the surface of the body in the second accretion event (see Supplementary Material). We ran 10,000 two accretion events models with randomly chosen r_1, t_1, r_2 and t_2 values for a given κ value. The ranges of possible r_1 and t_1 values and the κ values were the same as the single accretion event model. The values of r_2 were chosen randomly between $r_1 + 1$ km and 500 km and the values of t_2 were chosen randomly between 2.0 - 4.5 Myr after CAI formation, reflecting the period during which the added material was variably metamorphosed, but not melted, by ^{26}Al decay.

At each timestep in both models, we calculated the values of the core temperature, T_c, the temperature of the magma ocean/bottom layer of the mantle, T_m, the radiogenic heat flux normalised to the surface area of the body, F_{rad}, the surface heat flux, F_s, the core-magma ocean/mantle boundary heat flux, F_{CMB}, the adiabatic core heat flux, F_{ad}, and the heat flux available to drive convection, $F_{drive} = F_{CMB} - F_{ad}$. Due to the cold surface temperature of an asteroid, we modelled a stagnant lid with variable thickness at the surface of our bodies across which heat is conducted. At high values of T_m, a partially-molten, isothermal magma ocean exists across part of the silicate portion of the body that can convect heat to the base of the lid. We calculate the thermally-driven magnetic Reynolds number, $Re_{m,therm}$, from our calculated thermal evolutions (see Supplementary Material), which indicates whether convection was sufficiently vigorous to generate magnetic fields. A value of $Re_{m,therm} \geq 10$ has been proposed for field generation within asteroid-sized bodies, which is thought to have been the case for relatively large F_{CMB} values ($\gtrsim$0.1 W m^{-2}; Weiss et al., 2010). This heat flux is most easily achieved if heat is convected away from the core (e.g, Evans et al., 2014), so model the magma ocean in our bodies as extending to the base of the silicate portion of the body. It is possible that upward melt migration during differentiation could limit the depths of magma oceans in some bodies (e.g., Vesta; Neumann et al., 2014), which could effect their generation and timing of thermally-driven dynamo activity.

3. Results

3.1. General results from the single accretion events model

The evolutions of T_m, T_c, F_s, F_{rad}, F_{CMB}, F_{ad} and $Re_{m,therm}$ calculated from our single accretion event model with representative parameters ($t_1 = 0.5$ Myr after CAI formation, $r_1 = 400$ km, $\kappa = 9 \times 10^{-7}$ m^2 s^{-1}) are shown in Fig. 1. The broad, qualitative trends in these properties are typical of those calculated from all our random parameter combinations in our single accretion event model. Below we outline the thermal history of this body, which we present in four stages defined by its thermal and dynamic evolution. The timings we state are specific to the parameter combination in the body in Fig. 1 and the trends in these timings across our ranges of parameter combinations are presented at the end of this section.

In stage 1, the body heats up to its differentiation temperature through the radioactive decay of ^{26}Al. Differentiation has been proposed to occur at temperatures below the 50% silicate melting temperature if the body experienced a shear stress that facilitated the segregation of molten metal from silicate (e.g., Berg et al., 2017). Therefore, differentiation occurs in our model at the temperature that the Rayleigh number of the body, Ra_m, increased above the critical Rayleigh number, Ra_c, (typically ∼1450 - 1550 K) corresponding to the time the body starts convecting and experiencing this stress. Stage 1 lasts until 0.74 Myr after CAI formation (Fig. 1a). During differentiation, we model the body as instantaneously separating into a molten core and a partially-molten magma with a thin stagnant lid at its surface.

In stage 2, which lasts between 0.74 - 0.91 Myr after CAI formation (Fig. 1a), the magma ocean continues to heat up and convect heat upward throughout the body. The lithophilic nature of Al causes all the ^{26}Al still present at the time of differentiation to partition into the silicate portion of the body, meaning only this portion continues to produce heat. This heat passes from the magma ocean into the core, causing T_c to increase, and into the lid, where it is conducted to the surface and radiated into space. Stage 2 ends when T_c exceeds T_m.

In stage 3, the partially-molten magma ocean cools and convects heat upward throughout the body. At T_m >1600 K, the magma ocean has a low viscosity (Fig. S2 in Supplementary Material), leading to efficient heat loss from the body. This heat loss balances radiogenic heat production (Fig. 1b), keeping T_m and T_c

essentially isothermal at a temperature just above 1600 K, creating small values of F_{CMB} (early portion of stage 3). Once heat production slows, the magma ocean starts cooling and the temperature difference between the core and magma ocean increases, causing F_{CMB} to increase (middle portion of stage 3). As the magma ocean cools further, its viscosity and the stagnant lid thickness increase, causing a corresponding decrease in F_{CMB} (later portion of stage 3, Fig. 1b). As the lid grows, the distance over which convection occurs in the magma ocean decreases, causing Ra_m to decrease. At a critical solid thickness ($\sim$160 km in Fig. 1), which is reached $\sim$21.5 Myr after CAI formation, Ra_m falls below Ra_c and the mechanism of heat transfer within the magma ocean transitions from convection to conduction and stage 3 ends.

In stage 4, heat is conducted throughout the entire silicate portion of the body. The remaining magma ocean is isothermal and $\sim$40 K colder than the core when it transitions from convective to conductive heat transport. This temperature difference is quickly removed by the conduction of heat across the core-magma ocean boundary, causing a very short-lived spike in F_{CMB} after which the base of the magma ocean and the core become essentially isothermal again. As surface cooling continues, the thickness of which heat is conducted towards the surface increases (early portion of stage 4) until it reaches the core-mantle boundary at $\sim$100 Myr after CAI formation and the core starts cooling by conduction. Before conductive core cooling, core cooling effectively pauses and F_{CMB} is sub-adiabatic. Positive F_{CMB} values are re-introduced once conductive core cooling starts, however they are smaller than those achieved by convection during stage 3.

In our model, eutectic core solidification occurs at the end of stage 4 once the core cools to 1200 K. The core is kept isothermal by the release of latent heat. In reality, the S concentrations of most asteroids cores suggest they could have started solidifying at a wide range of times spanning stages 3 and 4. If core solidification begins during stage 3 (low S concentrations), we expect it pauses when core cooling pauses when the magma ocean transitions from convective to conductive heat transfer. Core solidification either restarts or, in the case of high S concentrations, starts during stage 4 once the core starts cooling by conduction. Our model predicts that the core was entirely solid $\sim$492 Myr after CAI formation.

The values of F_{drive} and $Re_{m,therm}$ are negative immediately after differentiation as the magma ocean heats up and passes heat into the core (stage 2 in Fig. 1c). The subsequent near-isothermal core and magma ocean (early portion of stage 3) causes low, positive values of F_{drive} and $Re_{m,therm}$. Once the magma ocean starts cooling and F_{drive} increases, $Re_{m,therm}$ becomes >10 and we predict a period of thermally-driven dynamo activity starting ~5.0 Myr after CAI formation. As F_{drive} decreases, $Re_{m,therm}$ also decreases and falls <10 at ~9.7 Myr after CAI formation, leading to a predicted ~4.7 Myr period of thermally-driven dynamo activity (grey bar in stage 3, Fig. 1c).

The pause in core cooling at the beginning of stage 3 causes negative values of F_{drive} and $Re_{m,therm} = 0$ (early part of stage 4). A positive F_{drive} and non-zero value of $Re_{m,therm}$ are re-introduced when heat starts being conducted from the core (middle part of stage 4). However, $Re_{m,therm}$ remains sub-critical during this period due to the relatively low F_{drive} values and we do not predict a period of conductive thermally-driven dynamo activity during this stage.

Uncertainties in the direction and temperature of asteroid core solidification make the timing of compositionally-driven dynamo activity difficult to predict. However, modelling the core as solidifying outwards (see Supplementary Material), this process could produce values of compositionally-driven magnetic Reynolds number, $Re_{m,comp}$, that are much larger than $Re_{m,therm}$ and can be >10 for a portion of core solidification for bodies with r_1 as small as 50 km (Fig. S3 in the Supplementary Material). The portion of core solidification that generates super-critical $Re_{m,comp}$ values likely increases with core radius. Therefore, compositionally-driven dynamo activity could possibly have been generated for at least a portion of core solidification, however we are unable to predict its timing. It is possible this activity could start at a wide range of times spanning stage 3 or 4 depending on the initial core S concentration and could possibly last tens of Myr. We also expect that compositionally-driven dynamo activity paused for possibly tens of Myr when core cooling and solidification effectively paused as the magma ocean transitions heat transport mechanisms (earlier part of stage 4).

Models that span our ranges of r_1 and t_1 values with $\kappa = 9 \times 10^{-7}$ m^2 s^{-1} demonstrate that both the start time and duration of thermally-driven dynamo activity depend primarily on the radius of the body (Fig. 2). Thermal dynamo activity is delayed systematically until 5.0 - 5.7 Myr after CAI formation and lasts <12.5 Myr for the range of r_1 values we modelled. Bodies with $r_1 \lesssim 340$ km and $t_1 \gtrsim 1.7$ Myr after CAI did not generate $Re_{m,therm} > 10$ for the parameters in our models. Bodies with larger thermal diffusivities produce earlier and shorter-lived thermal dynamo activity for a given radius, reflecting the faster transfer of heat throughout these bodies (Fig. S4a in the Supplementary Material). The timing of the end of core solidification also depends systematically on the radius of the body, spanning times between ∼10 - 750 Myr (Fig. 3). Similar to thermal dynamo activity, bodies with higher thermal diffusivities also produce earlier end times of core solidification (Fig. S4b in the Supplementary Material).

3.2. General results from the two accretion event model

The evolutions of T_m, T_c, F_s, F_{rad}, F_{CMB}, F_{ad} and $Re_{m,therm}$ calculated from our two accretion event model with representative parameters ($t_1 = 0.5$ Myr after CAI formation, $t_2 = 3.0$ Myr after CAI formation, $r_1 = 400$ km, $r_2 = 500$ km, $\kappa = 9 \times 10^{-7}$ m^2 s^{-1}) are shown in Fig. 4. Here, F_s is the heat flux out of the surface of the molten portion of the body into the cold chondritic material added during the second accretion event.

The general trends in these temperature, fluxes and $Re_{m,therm}$ are similar to those calculated in our single accretion event model. We predict that bodies that form through two-stage accretion still produce an initial period of dynamo quiescence during differentiation, magma ocean heating and near-isothermal magma ocean and core (stages 1, 2 and earlier part of 3), followed by a brief period of thermally-driven dynamo activity as heat is convected across a partially-molten magma ocean (middle part of stage 3). We also expect periods of compositional convection driven by core solidification that could start at times spanning stages 3 and 4 depending on the core S concentration that pauses for possibly tens of Myr after heat starts being conducted throughout the magma ocean (earlier part of stage 4).

The timings of both thermally-driven dynamo activity and the end of core solidification in our two accretion event models are also governed predominantly by r_1 (Figs. 5, 6, S7 and S8 in the Supplementary Material). The end time of core solidification also depends on r_2 as the addition of chondritic material can further insulate the core and delay this process (Fig. S8 in the Supplementary Material). The predicted timing of both thermally-driven dynamo activity and the end of core solidification also display some scatter due to changes in the degree of core insulation and core radius caused by the addition and melting of the material in the second accretion event, respectively. The melting of this material can also increase the core radius in bodies with relatively small r_1 values, permitting some of these bodies to generate thermally-driven dynamo activity. Again, the timings of thermally-driven dynamo activity and the end of core solidification are earlier and shorter for bodies with higher thermal diffusivities (Fig. S5 in the Supplementary Material).

The thermal evolutions at various depths throughout the added chondritic material are shown in Fig. 7a. The material at the base of the added chondritic material (100 km deep) partially melts soon after it is added due to its proximity to the partially-molten interior of the body. The chondritic material at depths of 75 and 50 km experiences some interior heating that increases its temperature less and occurs later than radiogenic heating. The thermal evolutions at depths of 25 km and 5 km are not noticeably affected by interior heating. Material at depths $\lesssim$89 km does not partially melt and it retains its chondritic nature. This body is therefore partially differentiated, consisting of an unmelted exterior atop a molten interior. The percentage thickness of the added chondritic material that does not melt as functions of the thickness of the added material and t_2 is shown in Fig. 7b. Chondritic material added at earlier t_2 times experiences more radiogenic heating, so less heat from the interior is required for this material to melt. A significant portion of the added chondritic material can melt for bodies with $t_2 < 2.5$ Myr after CAI formation, although partially differentiated bodies can still form at this time if enough chondritic material is added.

4. Comparison of model predictions and the asteroid magnetic field record

4.1. General comparisons

A record of asteroid magnetic activity compiled from paleomagnetic measurements of multiple meteorites is shown in Fig. 8. Although these meteorites originate from a number of parent bodies with different physical and chemical properties, this compilation still provides a broad overview of the evolution of asteroid magnetic activity.

Meteorites that recorded remanent magnetisations between 0 - 4 Myr after CAI formation, between 6 - 11 Myr after CAI formation, between ~80 - 140 Myr after CAI formation and the older pallasites experienced relatively intense magnetic fields (>2 μT). On the other hand, meteorites that recorded remanent magnetisations between 4 - 6 Myr after CAI formation, Allende chondrules that were aqueously altered ~40 Myr after CAI formation and the younger pallasites carry remanences that suggest they experienced fields with intensities too weak to impart a recoverable remanence, indicating they experienced weak or zero fields. Our solar nebula supported a magnetic field (Fu et al., 2014b) during the first ~3.8 - 4.8 Myr after CAI formation (Wang et al., 2017). Assigning remanent magnetisations carried by material that dates from 0 - 4 Myr after CAI formation (Semarkona chondrules and CM chondrites) to this field leaves a trend in the recovered paleointensities that is consistent with our predicted timings of dynamo activity generation. The thermal remanent magnetisations (TRMs) carried by the volcanic angrites Sahara 99555 and D'Orbigny (Wang et al., 2017) and the ungrouped achondrite NWA 7325 (Weiss et al., 2017) as well as the aqueous chemical remanent magnetisation (CRM) measured in the Kaba CV chondrite (Gattacceca et al., 2016) were recorded between ~4 - 6 Myr after CAI formation and correspond to paleointensities <1.7 µT. We assign these weak remanences to the absence of dynamo activity following differentiation in their parent bodies. The TRMs measured in the plutonic angrite Angra dos Reis (Wang et al., 2017), Kaba (Gattacceca et al., 2016) and the Allende CV chondrite (Carporzen et al., 2011) as well as the shock-induced remanence in the Vigarano CV chondrite (Shah et al., 2017) were acquired between ~6 - 11 Myr after CAI formation and are relatively intense (paleointensities >3 µT). We assign the likely origin of these remanences to thermally-driven dynamo activity generated by the convection of heat from the cores of their parent bodies. The weak CRM in individual Allende chondrules ($\lesssim$8 µT; Fu et al., 2014a) acquired ~40 Myr after CAI formation and the remanence carried by the older pallasites Marjalahti and Brenham (probably <1 µT; Nichols et al., 2016; Maurel et al., 2019) possibly recorded sometime between ~100 - 150 Myr after CAI formation are consistent with our prediction that dynamo activity pauses after heat starts being conducted through the silicate portions of their parent bodies. The paleointensities recovered from Allende chondrules are also consistent with a weak dynamo field, which could be the case if the CV parent body was generating compositionally-driven dynamo activity at ~40 Myr after CAI formation (see Supplementary Material). The stronger remanences in the H6 chondrite Portales Valley (Bryson et al., in press) and the IIE iron meteorite Colomera (Maurel et al., 2018), both acquired at ~100 Myr after CAI formation, as well as that in the L/LL chondrite Bjürbole (likely recorded sometime between 80 - 140 Myr after CAI formation; Shah et al., 2017) and the younger pallasites Imilac and Esquel (possibly recorded sometime between ~180 - 250 Myr after CAI formation; Bryson et al., 2015; Tarduno et al., 2012) all correspond to paleointensities $\gtrsim$5 µT, which we ascribe to compositionally-driven magnetic fields induced by core solidification.

4.2. Angrite parent body properties

The timing of dynamo generation in an asteroid depends on its radius (Figs. 2, 3, 5 and 6), so periods of dynamo presence and absence recovered from paleomagnetic measurements of meteorites with reliable remanence acquisition ages could be used to constrain the size of their parent bodies. The radii we draw from the timing of thermally-driven dynamo activity (i.e., regarding the angrite and CV parent bodies) depend on the rotation period of the bodies. Possible values of this parameter span tens of hours, which can change the recovered radii by up to ~100 km.

The angrites are a group of basaltic achondrites that originate form a differentiated asteroid. The volcanic angrites experienced paleointensities <0.6 µT at ~3.8 - 4.8 Myr after CAI formation and the plutonic angrites experienced paleointensities of ~17 µT at ~11 Myr after CAI formation. Assuming the field recorded by the plutonic angrites was generated by thermal convection, we can constrain the size of the angrite parent body by identifying examples of our single accretion event model with $\kappa = 9 \times 10^{-7}$ m^2 s^{-1} that produced thermally-driven dynamo activity starting >3.8 Myr after CAI formation and ceasing >11 Myr after CAI formation, which is the case for models with $r_1 > 420$ km (Fig. 9a). It is also feasible that the field recorded by the plutonic angrites was generated by compositional-convection induced by early core solidification. However, given the unknown freezing temperature and solidification direction of the angrite parent body core, the only constraint we can reliably draw in this scenario is the range of r_1 values that produce bodies with at least partially molten cores at 11 Myr after CAI formation that could feasibly have been generating a field at this time. This range corresponds to $r_1 > 60$ km (Fig. S4b). The uncertainties surrounding the timing of compositionally-driven convection make this constraint less reliable than that drawn from the timing of thermally-driven convection. The radius of the angrite parent body has recently been independently estimated from the volatile content of melt inclusions within the angrites as >270 km

(Sarafian et al., 2017), which agrees with our radius range recovered from the timing of thermally-driven convection.

4.3. CV chondrite parent body properties

The CV chondrites are a group of mildly aqueously altered and moderately heated (~150 °C - <600 °C depending on the meteorite) carbonaceous chondrites. This thermal and alteration history means these meteorites can carry both a TRM and a CRM. The Kaba and Allende CV chondrites carry TRMs acquired in fields with paleointensities of ~3 µT at >4 - 6 Myr after CAI formation and ~60 µT at $\gtrsim$9 Myr after CAI formation, respectively (Gattacceca et al., 2016; Carporzen et al., 2011). These meteorites also carry weak CRMs acquired in fields with paleointensities of <0.3 µT at some time between ~4 - 6 Myr and <8 µT at ~40 Myr after CAI formation, respectively (Gattacceca et al., 2016; Fu et al., 2014a). The Vigarano CV chondrite recorded a remanence as it was shocked and brecciated at ~9 Myr after CAI formation (Shah et al., 2017). The ages and durations of remanence acquisition have been used to argue that these TRMs and the shock-induced remanence are records of a dynamo field, suggesting the CV parent body was partially differentiated (Elkins-Tanton et al., 2011). Given the uncertainties surrounding the timing and mechanisms of compositionally-driven convection and whether Allende chondrules actually experienced a field (see Supplementary Material), we simply inferred the properties of the CV parent body from our two accretion event models with $\kappa = 6 \times 10^{-7}$ m^2 s^{-1} that were producing thermally-driven dynamo activity by 6 Myr and were still producing this activity at 9 Myr after CAI formation. We find that bodies with $r_1 >$ 220 km and $r_2 >$ 400 km satisfy these criteria (Fig. 9b).

4.4. H chondrite, Bjürbole and IIE iron meteorite parent body properties

The siderophile elements concentration and oxygen isotope systematics suggest that the IIE iron meteorites originate from pools of molten metal in the mantle of a H-chondrite-like asteroid (Weiss and Elkins-Tanton, 2013). Synchrotron microscopy measurements indicate that the Portales Valley H6 chondrite and Colomera IIE iron meteorite both experienced fields with paleointensities of ~10 - 20 µT at ~100 Myr after CAI formation (Bryson et al., in press; Maurel et al., 2018). The age and longevity of these fields are uniquely consistent with young, compositionally-driven dynamo activity, which, coupled with the presence of melted and unmelted silicates in the IIE iron meteorites, implies the H chondrite and IIE iron parent bodies were partially differentiated. We therefore constrained the properties of these bodies from our two accretion event models with $\kappa = 9 \times 10^{-7}$ m^2 s^{-1} that had core solidification ending >100 Myr after CAI formation so could feasibly have been generating fields when Portales Valley and Colomera recorded their remanences. We also adopted the criterion that $t_2 < 2.5$ Myr after CAI formation to explain the peak metamorphic temperatures inferred from the H chondrites and IIE silicates. We find that $r_2 > 170$ km matches these criteria (Fig. 9c). The radius of the H chondrite parent body has recently been independently constrained to >130 - 140 km based on Pb-Pb ages of multiple H chondrites (Blackburn et al., 2017), which agrees with our proposed ranges.

We adopted a similar approach to recover the radius of the Bjürbole (L/LL chondrite) parent body. This meteorite experienced a field likely at some time between 80 - 140 Myr after CAI formation. The cores of partially differentiated bodies with $r_2 > 150$ km and $r_2 > 200$ km are at least partially molten at the lower and upper limits of this period, respectively.

4.5. Source of magnetic remanence in the CM chondrites

The CM chondrites are weakly metamorphosed and extensively aqueously altered meteorites. They carry uniform CRMs imparted by a weak field (4 ± 3 μT; Cournede et al., 2015), which has been suggested to have been either the stable, out-of-disk component of the nebula field or a weak dynamo field if the CM parent body was partially differentiated.

The age of remanence acquisition in the CM chondrites was coeval with magnetite formation (Cournede et al., 2015). However, a reliable magnetite formation age in the CM chondrites has yet to be published. Pravdivtseva et al. (2018) recently presented a magnetite I-Xe age in the CI chondrites of 2.9 ± 0.3 Myr after CAI formation, which is likely the oldest possible age of magnetite in the CM chondrites given the contemporaneous Mn-Cr carbonate formation ages in these two groups and the lower degree of aqueous alteration in most CM meteorites (Fujiya et al., 2012, 2013). This observation also suggests the chondritic portion of the CM parent body likely accreted $\gtrsim$3.0 Myr after CAI formation. Our two accretion event models with $\kappa = 6 \times 10^{-7}$ m^2 s^{-1}and $t_2 > 3.0$ Myr after CAI formation demonstrate that thermally-driven dynamo is delayed until >5 Myr after CAI formation (Fig. 9d) making it is unlikely that the remanence in these meteorites was imparted by a dynamo field. Instead, it is far more likely that these meteorites were magnetised by the stable component of the nebula field. Models of this field indicate that its intensity decreased from ∼6 - 1 μT between heliocentric distances of 2 - 5 AU (Bai, 2015), consistent with the paleointensities recovered from the CM chondrites.

5. Conclusions

- The properties of planetary magnetic fields generated by core dynamo activity provide a window into the internal thermal and dynamic behaviour of a planetary body. Paleomagnetic measurements of ancient samples can therefore provide constraints on the thermochemical history of their parent bodies.

- We conducted models of the thermal evolution of asteroid-sized bodies with the aim of predicting when they generated dynamo fields. These simulations covered the entire active lifetime of an asteroid core, considered multiple field generation mechanisms and included a suite of planetary radii, accretion times and thermal diffusivities. We modelled the evolution of both fully differentiated bodies that formed through a single accretion event and partially differentiated bodies that formed through two accretion events.

- We predict various epochs of magnetic field generation. Dynamo activity is delayed until ∼4.5 - 5.5 Myr after CAI formation as the silicate portion of a body heats up after differentiation, followed by a short-lived (<12.5 Myr for the size of bodies in our models) period of thermally-driven dynamo activity as heat is convected across a partially-molten magma ocean. Depending on the core S concentration, core solidification and compositionally-driven dynamo activity could start at any time over the next few tens to hundreds of Myr. We predict a quiescent period of dynamo activity after heat starts being conducted throughout the silicate portion of a body. The timing of dynamo activity depends on the radius of the body.

- These predicted periods of dynamo absence and generation match periods of low and high paleointensities in the asteroid magnetic field record compiled from paleomagnetic measurements of multiple meteorites. Our models allow us to interpret this record by suggesting the possible mechanisms that generated the fields that imparted the remanent magnetisation to these meteorites.

- We used the timing of field generation recovered from the angrites, CV chondrites, H chondrites, IIE iron meteorites and Bjürbole to constrain the radii of their parent bodies. Our values are similar to previous independent estimates of these parameters. Our models also indicate that the CM chondrites were likely magnetised by the nebula field rather than a dynamo field.

Acknowledgements

JFJB would like to thank St. John's College, University of Cambridge for funding. JAN is partially funded by a Royal Society University Research Fellowship. We would like to thank Richard Harrison for helpful discussions and an anonymous reviewer who helped improve the quality of the manuscript.

Parameter	Symbol	Value	Unit	Reference
Heating rate of ^{26}Al at t = 0	h_o	0.355	$W\,kg^{-1}$	Elkins-Tanton et al. (2011)
^{26}Al/^{27}Al in accreting material at t = 0	Al_o	5×10^{-5}		Elkins-Tanton et al. (2011)
Abundance of Al in accreting material	X_{Al}	1.4	$wt\%$	Doyle et al. (2015)
Half-life of ^{26}Al	t_{half}	0.717	Myr	Neumann et al. (2014)
Surface temperature	T_s	200	K	Henke et al. (2013)
Melting temperature of accreting material	T_{melt}	1600	K	Bryson et al. (2015); Tarduno et al. (2012)
Reference viscosity	η_o	1×10^{21}	$Pa\,s$	Sterenborg and Crowley (2013)
Activation energy	E	300	$kJ\,mol^{-1}$	Sterenborg and Crowley (2013)
Reference temperature	$T_{o,\eta}$	1400	K	Sterenborg and Crowley (2013)
Thermal expansivity of silicate material	α_m	4×10^{-5}	K^{-1}	Sterenborg and Crowley (2013)
Thermal diffusivity of silicate material	κ	3×10^{-7}, 6×10^{-7}, 9×10^{-7}, 12×10^{-7}	$m^2\,s^{-1}$	Opeil et al. (2012)
Density of silicate material	ρ_m	3000	$kg\,m^{-3}$	Elkins-Tanton et al. (2011)
Heat capacity of silicate material	$C_{p,m}$	800	$J\,kg^{-1}\,K^{-1}$	Elkins-Tanton et al. (2011)
Latent heat of mantle material	L_m	400	$kJ\,kg^{-1}$	Elkins-Tanton et al. (2011)
Density of core material	ρ_c	7800	$kg\,m^{-3}$	Bryson et al. (2015)
Heat capacity of core material	$C_{p,c}$	850	$J\,kg^{-1}\,K^{-1}$	Elkins-Tanton et al. (2011)
Latent heat of core material	L_c	270	$kJ\,kg^{-1}$	Bryson et al. (2015); Tarduno et al. (2012)
Thermal conductivity of the core	k_c	30	$W\,m^{-1}\,K^{-1}$	Opeil et al. (2012)
Thermal expansivity of the core	a_c	9.2×10^{-5}	K^{-1}	Nimmo (2009)
Core freezing temperature	$T_{f,c}$	1200	K	Bryson et al. (2015); Tarduno et al. (2012)
Time step	δt	1×10^{11}	s	
Cell thickness	δr	500	m	
Core radius	r_c	Half the molten radius of body	m	
Characteristic length scale of convection	l	r_c	m	Nimmo (2009)
Magnetic diffusivity	λ	1.3	$m^2\,s^{-1}$	Weiss et al. (2010)
Density difference	$\Delta\rho$	195	$kg\,m^{-3}$	Bryson et al. (2015)
Nominal rotation period	p	36000	s	

Table 1: Parameters and values used in our models.

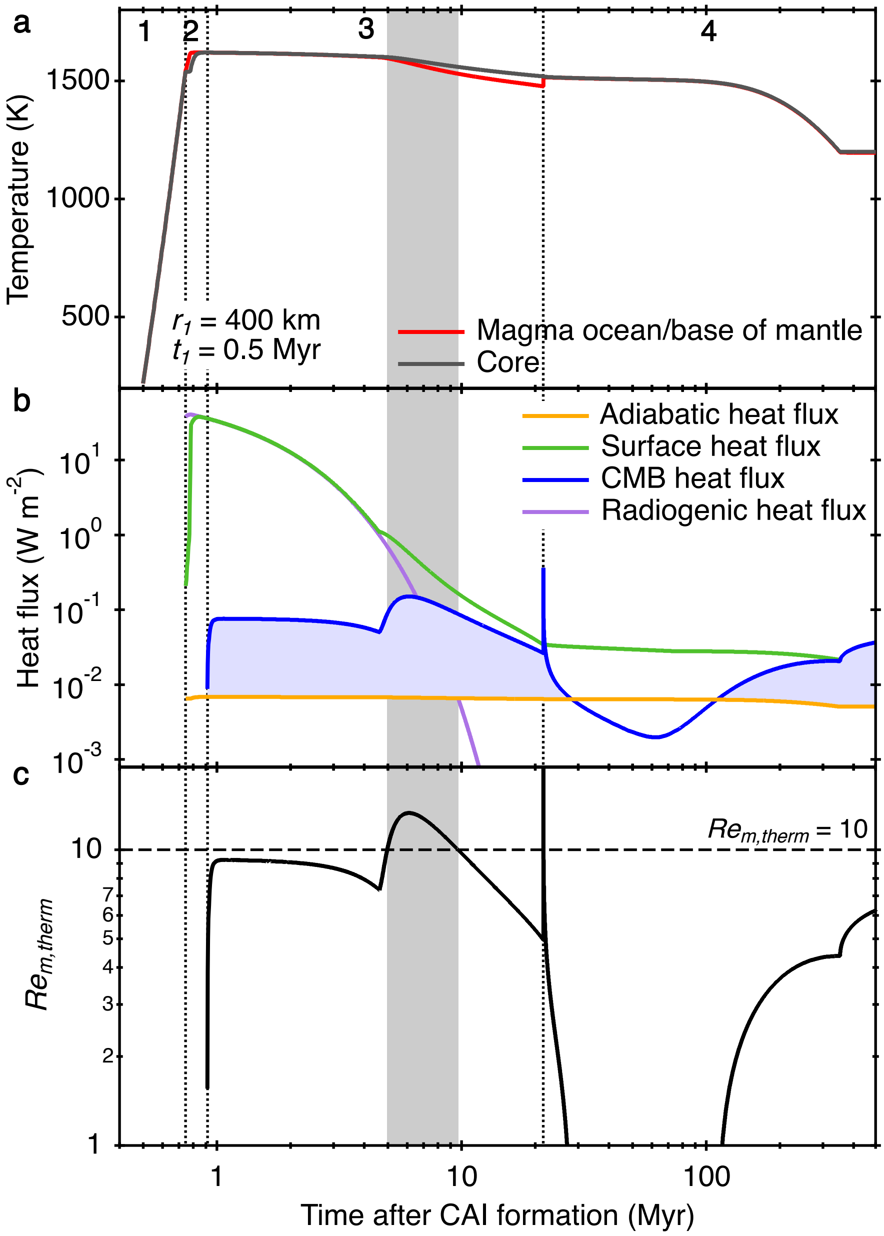

Figure 1: Results of our single accretion event model with $t_1 = 0.5$ Myr after CAI formation, $r_1 = 400$ km and $\kappa = 9 \times 10^{-7}$ m^2 s^{-1}. These trends are representative of the results of all of our single accretion event models. **a** The evolution of the temperature of the core and magma ocean/bottom layer of the solidified mantle. **b** The evolution of the adiabatic heat flux, surface heat flux and core-magma ocean/mantle boundary (CMB) heat flux. The light-blue shaded region represents F_{drive}. The radiogenic heat flux is normalised to the surface area of the body. **c** The evolution of $Re_{m,therm}$. Vertical dotted lines demarcate the different stages in our thermal evolution model, the horizontal dashed line marks $Re_{m,therm} = 10$ and the grey bars mark the predicted period of thermally-driven dynamo activity.

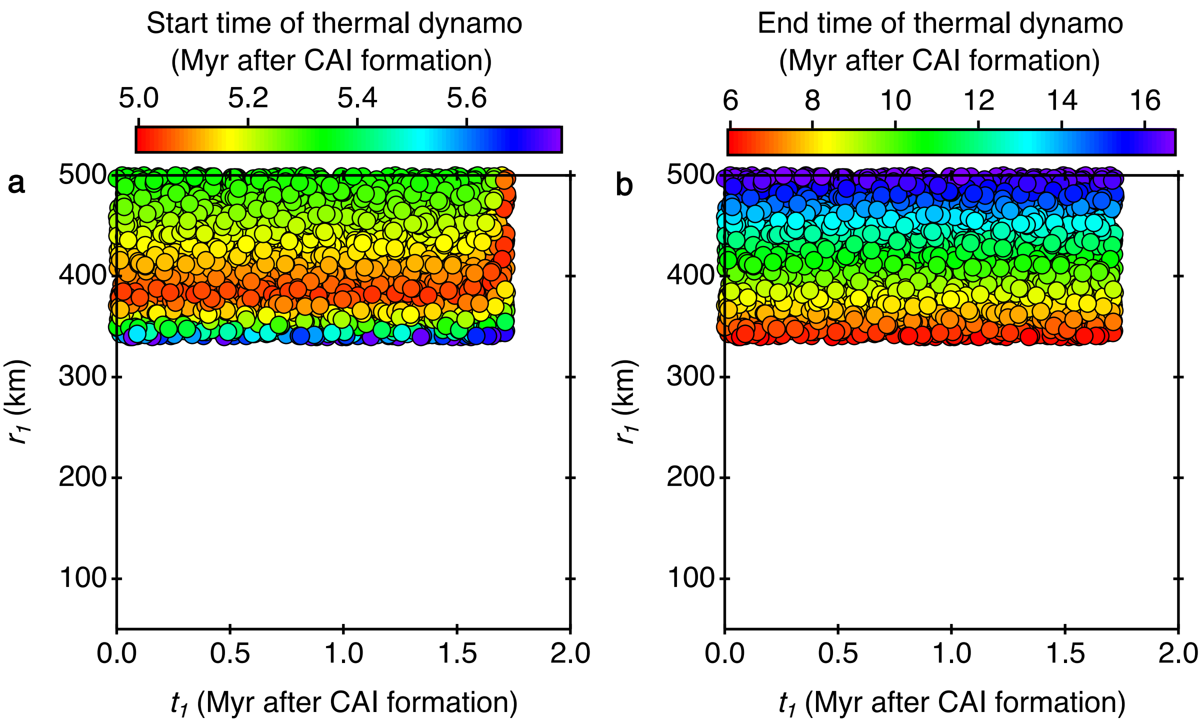

Figure 2: Predicted **a** start time and **b** end time of thermally-driven dynamo activity for our single accretion events model as functions of r_1 and t_1. White regions with no points represent parameter combinations that did not produce thermally-generated magnetic fields for the parameter values adopted in our models. We predict the timing of thermal dynamo activity depends predominately on r_1, which is shown in Figs. 9a and S4 in the Supplementary Material.

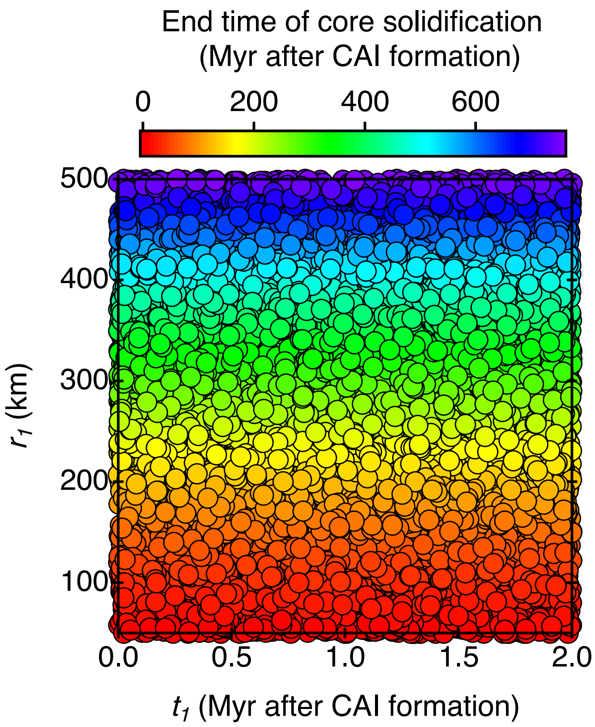

Figure 3: Predicted end time of core solidification for our single accretion events model as a function of r_1 and t_1.

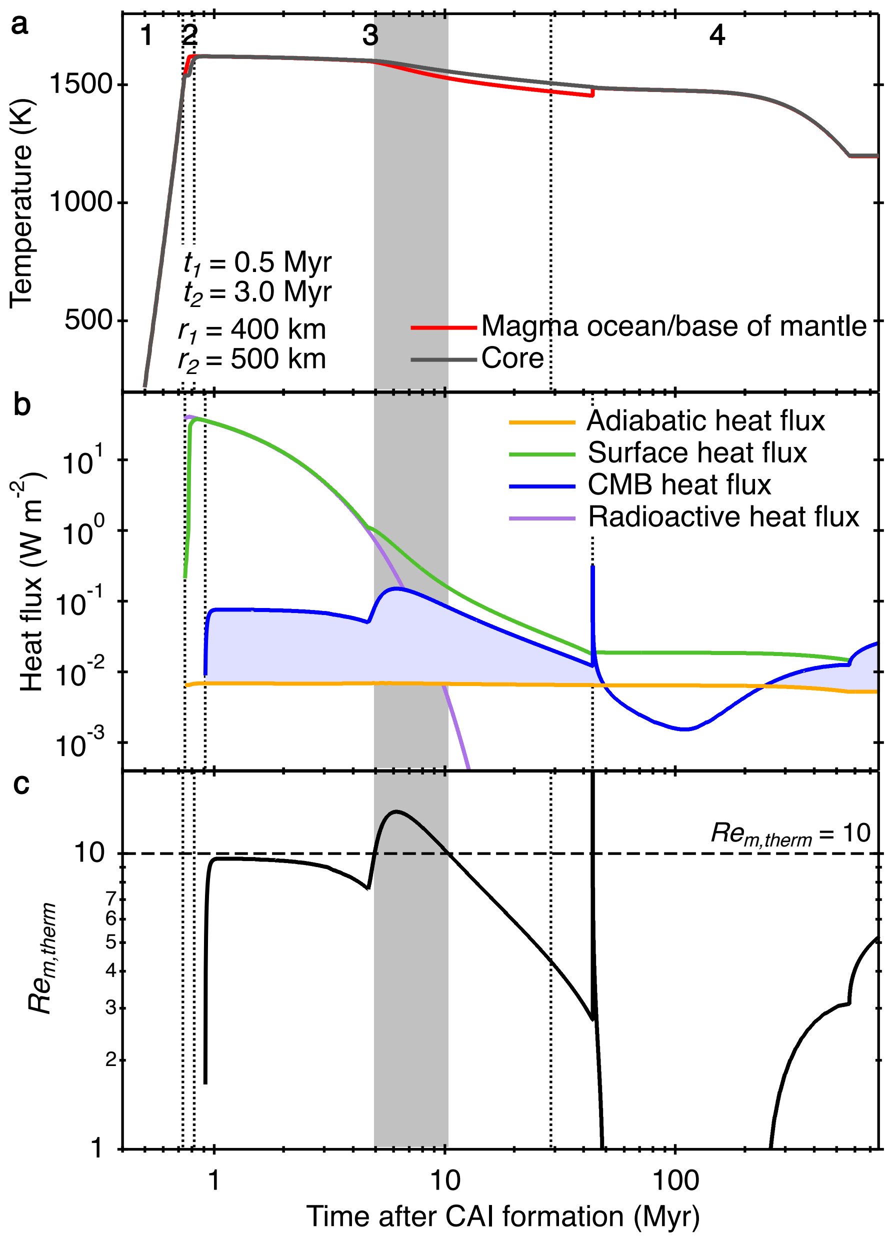

Figure 4: Results of our two accretion event model with $t_1 = 0.5$ Myr after CAI formation, $t_2 = 3$ Myr after CAI formation, $r_1 = 400$ km, $r_2 = 500$ km and $\kappa = 9 \times 10^{-7}$ m^2 s^{-1}. These trends are representative of the results of all of our two accretion event models. **a** The evolution of the temperature of the core and magma ocean/bottom layer of the solidified mantle. **b** The evolution of the adiabatic heat flux, surface heat flux and core-magma ocean boundary (CMB) heat flux. The light-blue shaded region represents F_{drive}. The radiogenic heat flux is normalised to the surface area of the molten portion of the body. **c** The evolution of $Re_{m,therm}$. Vertical dotted lines demarcate the different stages in our thermal evolution model, the horizontal dashed line marks $Re_{m,therm} = 10$ and the grey bars mark the predicted period of thermally-driven dynamo activity.

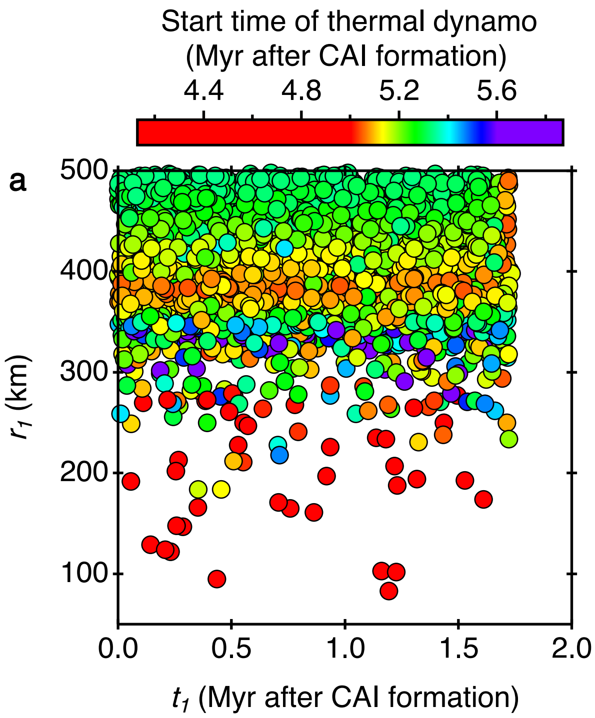

Figure 5: Predicted **a** start time and **b** end time of thermally-driven dynamo activity for our two accretion events model as a function of r_1 and t_1. White regions with no points represent parameter combinations that did not produce thermally-generated magnetic fields for the parameter values adopted in our models. We predict the timing of thermal dynamo activity depends predominately on r_1, which is shown in Figs. 9d and S5 in the Supplementary Material.

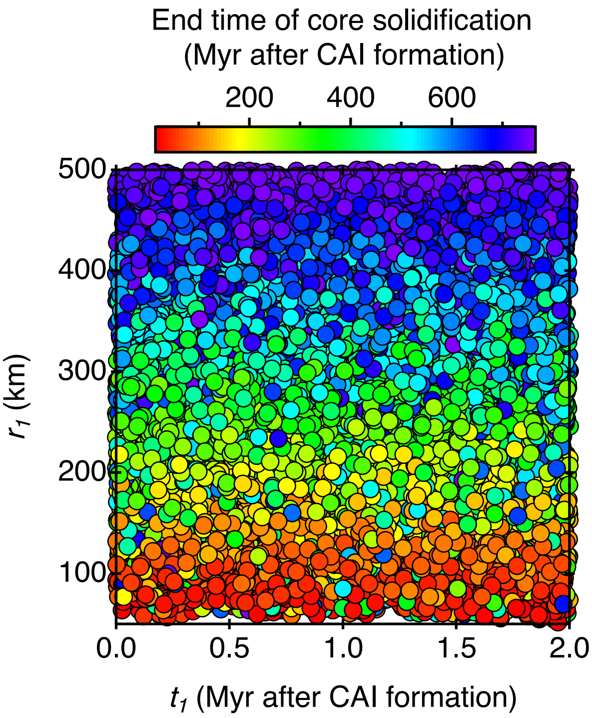

Figure 6: Predicted end time of core solidification for our two accretion events model as a function of r_1 and t_1.

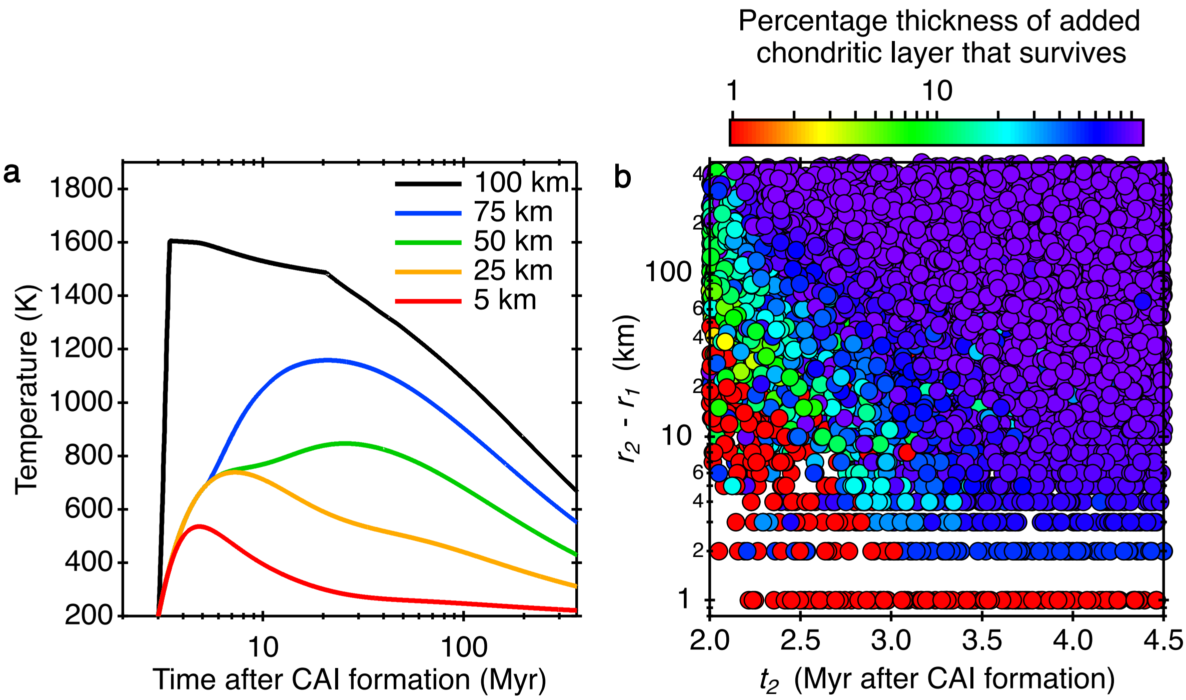

Figure 7: **a** Thermal evolution at depths of 100 km, 75 km, 50 km, 25 km and 5 km through the chondritic portion of a partially differentiated body with the same parameters as in Fig. 4. **b** Percentage thickness of the added chondritic material in our two accretion event models that survives metamorphism without melting as a function of total thickness of chondritic material added and t_2. More chondritic material survives at later t_2 values.

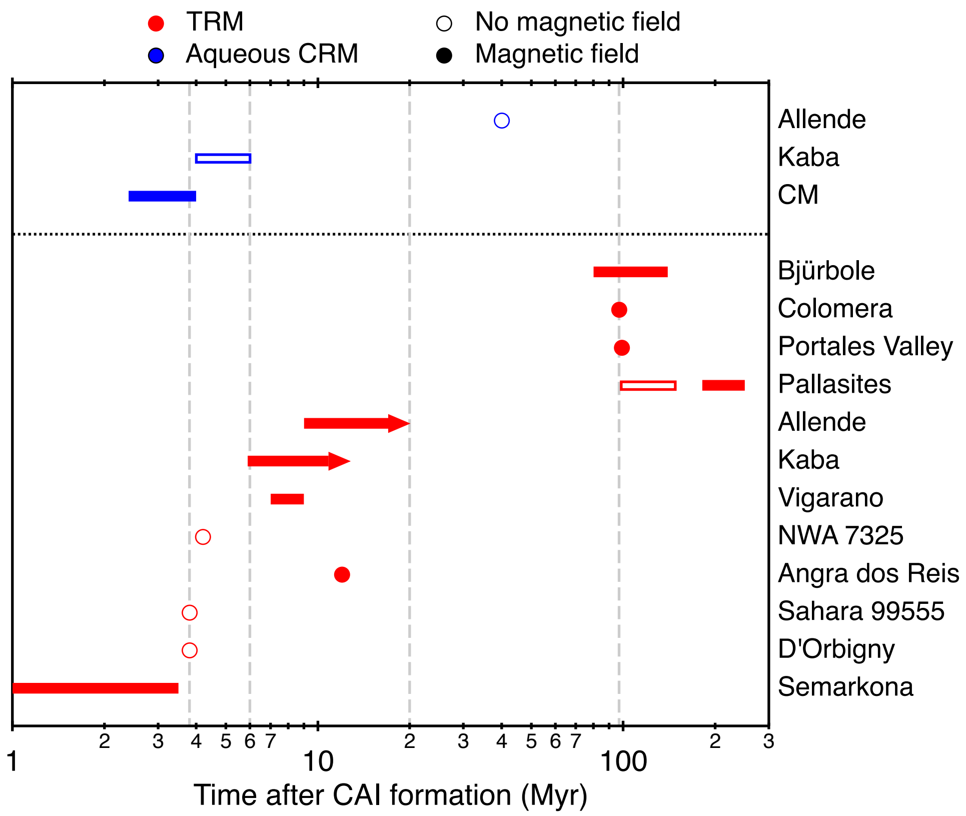

Figure 8: The asteroid magnetic field record compiled from the paleomagnetic measurements of multiple meteorites (Carporzen et al., 2011; Fu et al., 2014a,b; Cournede et al., 2015; Bryson et al., in press; Nichols et al., 2016; Gattacceca et al., 2016; Wang et al., 2017; Bryson et al., 2015; Weiss et al., 2017; Maurel et al., 2018; Shah et al., 2017). TRMs are shown in red and aqueous CRMs are shown in blue. Filled symbols represent samples that carry remanences indicating they experienced a field with intensity >2 μT and open symbols represent samples that experienced fields too weak for a recoverable remanence to be imparted, suggesting these samples experienced weak or zero field. Points represent reliably dated samples, bars represent age ranges inferred from dating measurements and arrows represent age limits inferred from dating measurements. Grey dashed lines demarcate the approximate eras of high and low recovered paleointensities.

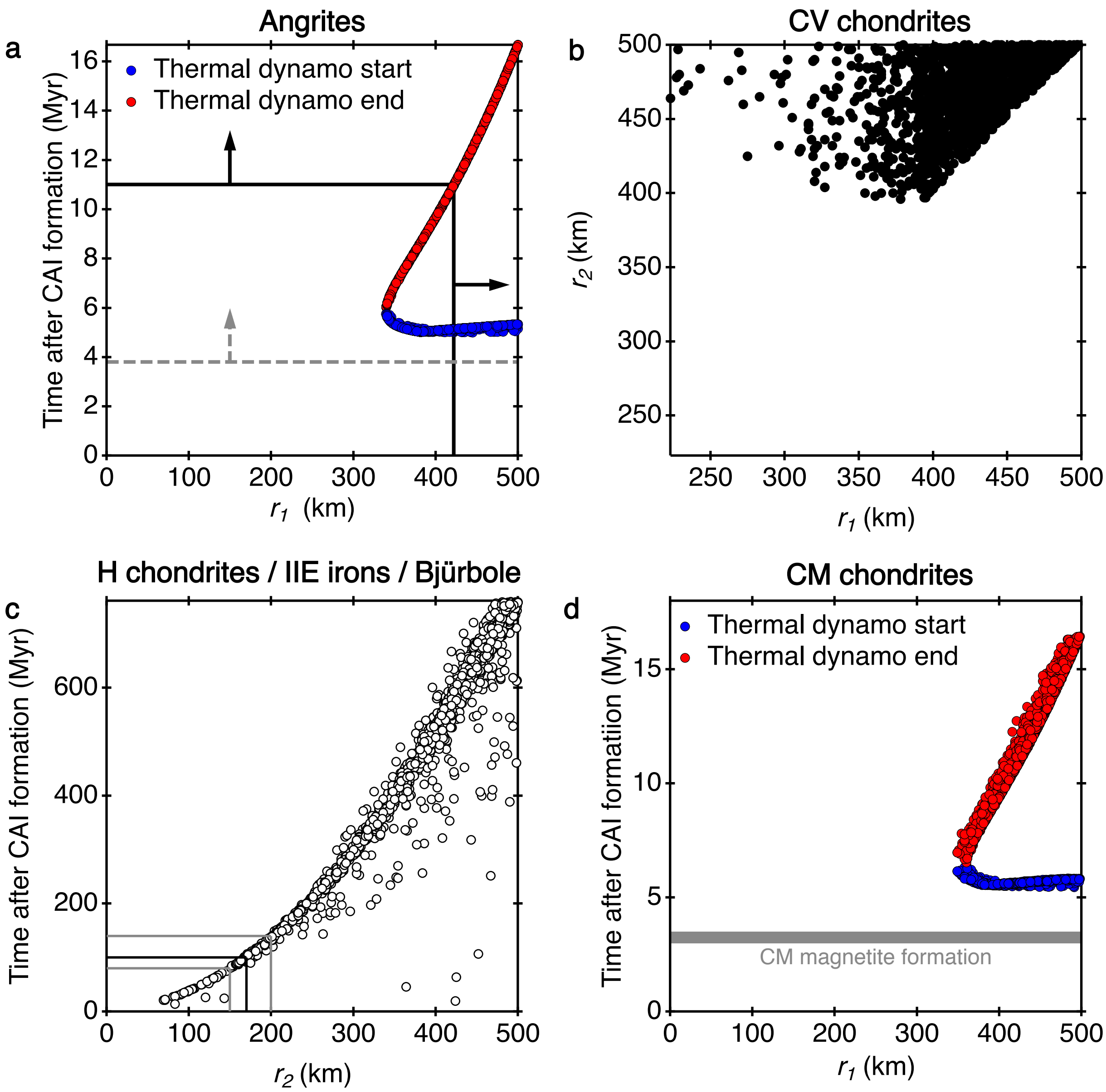

Figure 9: Parameter combinations that satisfy our criteria used to identify the properties of parent bodies of different meteorite groups. **a** Timing of the start and end of thermally-driven dynamo activity in our single accretion event models with the paleomagnetic constraints from the angrites included (thermal dynamo starts at >3.8 Myr after CAI formation [dashed grey line] and ends at >11 Myr after CAI formation [solid black lines]). Models with $r_1 > 420$ km satisfy these criteria. **b** Combinations of r_1 and r_2 from our two accretion event models that satisfy our criteria inferred from the CV chondrites (thermally-driven dynamo had started by 6 Myr after CAI formation and is still active at >9 Myr after CAI formation). **c** Timing of the end of core solidification in our two accretion event model with $t_2 < 2.5$ Myr with the paleomagnetic constraints from the H chondrite and IIE iron meteorites (core solidification ending at >100 Myr after CAI formation, black lines) and Bjürbole (core solidification ending at >80 - 140 Myr after CAI formation, grey lines). Models with $r_2 > 170$ km and $r_2 >$ 150 - 200 km satisfy these criteria, respectively. **d** Timing of the start and end of thermally-driven dynamo activity in our two accretion event models with $t_2 > 3.0$ Myr after CAI formation with the likely magnetite formation ages in the CM chondrites included. Our models started generating magnetic fields after time, indicating that the CM chondrites were likely magnetised by the field supported by our nebula (Bai, 2015) rather than a field generated by internal dynamo activity.

Bai, X. N., 2015. Hall effect controlled gas dynamics in protoplanetary disks. II. Full 3D simulations toward the outer disk. The Astrophysical Journal 798, 84.

Berg, M. T. L., Bromiley, G. D., Butler, I. B., Frost, M., Bradley, R., Carr, J., Le Godec, Y., Montési, L. G. J., Zhu, W., Miller, K., Perrillat, J. P., Mariani, E., Tatham, D., Redfern, S. A. T., 2017. Deformation-a-ided segregation of Fe-S liquid from olivine under deep earth conditions: Implications for core formation in the early solar system. Physics of the Earth and Planetary Interiors 263, 38–54.

Blackburn, T., Alexander, C. M. O., Carlson, R., Elkins-Tanton, L. T., 2017. The accretion and impact history of the ordinary chondrite parent bodies. Geochimica et Cosmochimica Acta 200, 201–217.

Bryson, J. F. J., Nichols, C. I. O., Herrero-Albillos, J., Kronast, F., Kasama, T., Alimadadi, H., van der Laan, G., Nimmo, F., Harrison, R. J., 2015. Long–lived magnetism from solidification–driven convection on the pallasite parent body. Nature 517, 472–475.

Bryson, J. F. J., Weiss, B. P., Getzin, B., Abrahams, J., Nimmo, F., Scholl, A., in press. Paleomagnetic evidence for a partially differentiated ordinary chondrite parent asteroid.

Bryson, J. F. J., Weiss, B. P., Harrison, R. J., Herrero-Albillos, J., Kronast, F., 2017. Paleomagnetic evidence for dynamo activity driven by inward crystallisation of a metallic asteroid. Earth and Planetary Science Letters 472, 152–163.

Carporzen, L., Weiss, B. P., Elkins-Tanton, L. T., Shuster, D. L., Ebel, D. S., Gattacceca, J., 2011. Magnetic evidence for a partially differentiated carbonaceous chondrite parent body. Proceedings of the National Academy of Sciences 108, 6386–6389.

Cournede, C., Gattacceca, J., Gounelle, M., Rochette, P., Weiss, B. P., Zanda, B., 2015. An early solar system magnetic field recorded in CM chondrites. Earth and Planetary Science Letters 410, 62–74.

Doyle, P. M., Jogo, K., Nagashima, K., Krot, A. N., Wakita, S., Ciesla, F. J., Hutcheon, I. D., 2015. Early aqueous activity on the ordinary and carbonaceous chondrite parent bodies recorded by fayalite. Nature Communications 6, 7444.

Elkins-Tanton, L. T., Weiss, B. P., Zuber, M. T., 2011. Chondrites as samples of differentiated planetesimals. Earth and Planetary Science Letters 305, 1–10.

Evans, A. J., Zuber, M. T., Weiss, B. P., Tikoo, S. M., 2014. A wet, heterogeneous lunar interior: Lower mantle and core dynamo evolution. Journal of Geophysical Research: Planets 119, 1061–1077.

Fu, R. R., Lima, E. A., Weiss, B. P., 2014a. No nebular magnetization in the Allende CV carbonaceous chondrite. Earth and Planetary Science Letters 404, 54–66.

Fu, R. R., Weiss, B. P., Lima, E. A., Harrison, R. J., Bai, X.-N., Desch, S. J., Ebel, D. S., Suavet, C., Wang, H., Glenn, D., Sage, D. L., Kasama, T., Walsworth, R. L., Kuan, A. T., 2014b. Solar nebula magnetic fields recorded in the Semarkona meteorite. Science 346, 1089–1092.

Fu, R. R., Weiss, B. P., Shuster, D. L., Gattacceca, J., Grove, T. L., Suavet, C., Lima, E. A., Li, L., Kuan, A. T., 2012. An ancient core dynamo in asteroid Vesta. Science 338, 238–241.

Fujiya, W., Sugiura, N., Hotta, H., Ichimura, K., Sano, Y., 2012. Evidence for the late formation of hydrous asteroids from young meteoritic carbonates. Nature Communications 3, 627.

Fujiya, W., Sugiura, N., Sano, Y., Hiyagon, H., 2013. Mn–Cr ages of dolomites in CI chondrites and the Tagish Lake ungrouped carbonaceous chondrite. Earth and Planetary Science Letters 362, 130–142.

Garrick-Bethell, I., Weiss, B. P., Shuster, D. L., Buz, J., 2009. Early lunar magnetism. Science 323, 356–359.

Gattacceca, J., Weiss, B. P., Gounelle, M., 2016. New constraints on the magnetic history of the CV parent body and the solar nebula from the Kaba meteorite. Earth and Planetary Science Letters 455, 166–175.

Goldstein, J. I., Scott, E. R. D., Chabot, N. L., 2009. Iron meteorites: Crystallization, thermal history, parent bodies, and origin. Chemie der Erde - Geochemistry 69, 293–325.

Henke, S., Gail, H. P., Trieloff, M., Schwartz, W. H., 2013. Thermal evolution model for the H chondrite asteroid - instantaneous formation versus protracted accretion. Icarus 226, 212–228.

Hevey, P. J., Sanders, I. S., 2006. A model for planetesimal meltdown by ^{26}Al and its implications for meteorite parent bodies. Meteoritics and Planetary Science 41, 95–106.

Johansen, A., Low, M. M., Lacerda, P., Bizzarro, M., 2015. Growth of asteroids, planetary embryos, and Kuiper belt objects by chondrule accretion. Science Advances 17, e1500109.

Johnson, C. L., Phillips, R. J., Purucker, M. E., Anderson, B. J., Byrne, P. K., Denevi, B. W., Feinberg, J. M., Hauck, S. A., Head, J. W., Korth, H., James, P. B., Mazarico, E., Neumann, G. A., Philpott, L. C., Siegler, M. A., Tsyganenko, N. A., Solomon, S. C., 2015. Low-altitude magnetic field measurements by MESSENGER reveal Mercury's ancient crustal field. Science 348, 892–895.

Lichtenberg, T., Golabek, G. J., Dullemond, C. P., Schönbächler, M., Gerya, T. V., Meyer, M. R., 2018. Impact splash chondrule formation during planetesimal recycling. Icarus 302, 27–43.

Maurel, C., Bryson, J. F. J., Weiss, B. P., Scholl, A., 2018. Paleomagnetic evidence for a layered partially differentiated iron–meteorite parent body. Lunar and Planetary Science Conference XLIX Abstract 1171.

Maurel, C., Weiss, B. P., Bryson, J. F. J., 2019. Meteorite cloudy zone formation as a quantitative indicator of paleomagnetic field intensities and cooling rates on planetesimals. Earth and Planetary Science Letters 513, 166–175.

Neufeld, J. A., Bryson, J. F. J., Nimmo, F., 2019. The top–down solidification of iron asteroids driving dynamo evolution. Journal of Geophysical Research: Planets.

Neumann, W., Breuer, D., Spohn, T., 2014. Differentiation of Vesta: Implications for a shalow magma ocean. Earth and Planetary Science Letters 395, 267–280.

Nichols, C. I. O., Bryson, J. F. J., Herrero-Albillos, J., Kronast, F., Nimmo, F., Harrison, R. J., 2016. Pallasite paleomagnetism: Quiescence of a core dynamo. Earth and Planetary Science Letters 441, 103–112.

Nimmo, F., 2009. Energetics of asteroid dynamos and the role of compositional convection. Geophysical Research Letters 36, L10210.

Opeil, C. P., Consolmagno, G. J., Safarik, D. J., Britt, D. T., 2012. Stony meteorite thermal properties and their relationship with meteorite chemical and physical states. Meteoritics and Planetary Science 47, 319–329.

Pravdivtseva, O., Krot, A. N., Hohenberg, C. M., 2018. I-Xe dating of aqueous alteration in the CI chondrite Orgueil: I. Magnetite and ferromagnetic separates. Geochimica et Cosmochimica Acta 227, 38–47.

Ruckriemen, T., Breuer, D., Spohn, T., 2015. The Fe snow regime in Ganymede's core: A deep–seated dynamo below a stable snow zone. Journal of Geophysical Research: Planets 120, 1095–1118.

Sarafian, A. R., Hauri, E. H., McCubbin, F. M., Lapen, T. J., Berger, E. L., Nielsen, S. G., Marschall, H. R., Gaetani, G. A., Righter, K., Sarafian, E., 2017. Early accretion of water and volatile elements to the inner Solar System: evidence from angrites. Philosophical Transactions of the Royal Society A 375.

Scheinberg, A. L., Elkins-Tanton, L. T., Schubert, G., Bercovici, D., 2016. Core solidification and dynamo evolution in a mantle–stripped planetesimal. Journal of Geophysical Research: Planets 121, 2–20.

Scott, E. R. D., 2007. Chondrites and the protoplanetary disk. Annual Review of Earth and Planetary Sciences 35, 577–620.

Shah, J., Bates, H. C., Muxworthy, A. R., Hezel, D. C., Russell, S. S., Genge, M. J., 2017. Long–lived magnetism on chondrite parent bodies. Earth and Planetary Science Letters 475, 106–118.

Sterenborg, M. G., Crowley, J. W., 2013. Thermal evolution of early solar system planetesimals and the possibility of sustained dynamos. Physics of the Earth and Planetary Interiors 214, 53–73.

Stevenson, D. J., 2010. Planetary magnetic fields: Achievements and prospects. Space Science Reviews 152, 651–664.

Tarduno, J. A., Cottrell, R. D., Nimmo, F., Hopkins, J., Voronov, J., Erickson, A., Blackman, E., Scott, E. R. D., McKinley, R., 2012. Evidence for a dynamo in the main group pallasite parent body. Science 338, 939–942.

Tarduno, J. A., Cottrell, R. D., Watkeys, M. K., Hofmann, A., Doubrovine, P. V., Mamajek, E. E., Liu, D., Sibeck, D. G., Neukirch, L. P., Usui, Y., 2010. Geodynamo, solar wind and magnetopause 3.4 to 3.45 billion years ago. Science 327, 1238–1240.

Tikoo, S. M., Weiss, B. P., Shuster, D. L., Suavet, C., Wang, H., Grove, T. L., 2017. A two–billion–year history for the lunar dynamo. Science Advances 3, e1700207.

Wang, H., Weiss, B. P., Bai, X.-N., Downey, B. G., Wang, J., Wang, J., Suavet, C., Fu, R. R., Zucolotto, M. E., 2017. Lifetime of the solar nebula constrained by meteorite paleomagnetism. Science 355, 623–627.

Warren, P. H., 2011. Ejecta-megaregolith accumulation on planetesimals and large asteroids. Meteoritics and Planetary Science 46, 53–78.

Weiss, B. P., Elkins-Tanton, L. T., 2013. Differentiated planetesimals and the parent bodies of chondrites. Annual Review of Earth and Planetary Sciences 41, 529–560.

Weiss, B. P., Fong, L. E., Vali, H., Lima, E. A., Baudenbacher, F. J., 2008. Paleointensity of the ancient Martian magnetic field. Geophysical Research Letters 35, L23207.

Weiss, B. P., Gattacceca, J., Stanley, S., Rochette, P., Christensen, U. R., 2010. Paleomagnetic records of meteorites and early planetesimal differentiation. Space Science Reviews 152, 341–390.

Weiss, B. P., Wang, H., Sharp, T. G., Gattacceca, J., Shuster, D. L., Downey, B., Hu, J., Kuan, A. T., Suavet, C., Irving, A. J., Wang, J., Wang, J., 2017. A nonmagnetic differentiated early planetary body. Earth and Planetary Science Letters 468, 119–132.

Williams, Q., 2009. Bottom–up versus top–down solidification of the cores of small solar system bodies: Constraints on paradoxical cores. Earth and Planetary Science Letters 284, 564–569.

Yomogida, K., Matsui, T., 1984. Multiple parent bodies of ordinary chondrites. Earth and Planetary Science Letters 68, 34–42.